

Stirring the false vacuum via interacting quantized bubbles on a 5564-qubit quantum annealer

Jaka Vodeb,^{1,*} Jean-Yves Desaulles,^{2,3,†} Andrew Hallam,³ Andrea Rava,^{1,4} Gregor Humar,^{5,6} Dennis Willsch,¹ Fengping Jin,¹ Madita Willsch,^{1,7} Kristel Michielsen,^{1,4,7} and Zlatko Papić^{3,‡}

¹*Jülich Supercomputing Centre, Institute for Advanced Simulation, Forschungszentrum Jülich, 52425 Jülich, Germany*

²*Institute of Science and Technology Austria (ISTA), Am Campus 1, 3400 Klosterneuburg, Austria*

³*School of Physics and Astronomy, University of Leeds, Leeds LS2 9JT, UK*

⁴*RWTH Aachen University, 52056 Aachen, Germany*

⁵*Department of Complex Matter, Jožef Stefan Institute, Jamova 39, 1000 Ljubljana, Slovenia*

⁶*Department of Physics, Faculty for Mathematics and Physics, Jadranska 19, University of Ljubljana, 1000 Ljubljana, Slovenia*

⁷*AIDAS, 52425 Jülich, Germany*

(Dated: June 24, 2024)

False vacuum decay is a potential mechanism governing the evolution of the early Universe, with profound connections to non-equilibrium quantum physics, including quenched dynamics, the Kibble-Zurek mechanism, and dynamical metastability. The non-perturbative character of the false vacuum decay and the scarcity of its experimental probes make the effect notoriously difficult to study, with many basic open questions, such as how the bubbles of true vacuum form, move and interact with each other. Here we utilize a quantum annealer with 5564 superconducting flux qubits to directly observe quantized bubble formation in real time – the hallmark of false vacuum decay dynamics. Moreover, we develop an effective model that describes the initial bubble creation and subsequent interaction effects. We demonstrate that the effective model remains accurate in the presence of dissipation, showing that our annealer can access coherent scaling laws in driven many-body dynamics of 5564 qubits for over $1\mu\text{s}$, i.e., more than 1000 intrinsic qubit time units. This work sets the stage for exploring late-time dynamics of the false vacuum at computationally intractable system sizes, dimensionality, and topology in quantum annealer platforms.

Nearly half a century ago, Coleman proposed the idea that our Universe may have cooled down into a metastable “false vacuum” state after the Big Bang and the time of tunneling to the ground state or “true vacuum” was estimated to be comparable to the lifetime of the Universe [1]. The idea was then further developed and applied to various cosmological observations and theories [2–8], with ongoing attempts to observe the signatures of false vacuum decay in gravitational waves [9].

The dynamics of false vacuum decay are believed to consist of “bubbles” of true vacuum forming in the background of false vacuum, where the size of a bubble is determined by balancing the energy gain proportional to the bubble volume and energy loss proportional to the bubble surface. Bubbles are typically assumed to undergo isolated quantum tunneling events, growing classically at a model-dependent speed [9]. The quantum process is difficult to study due to the non-perturbative nature of the dynamics. To circumvent this issue, early theoretical works have explored the possibility of directly creating new Universes in a laboratory setting [10] and in engineered platforms based on condensed matter systems [11]. With the advances in ultracold atomic gases, certain aspects of the false-vacuum decay dynamics can now be studied in table-top experiments [12].

Recently, there has been a flurry of interest in simulating quantum field theories using synthetic platforms of ultracold atoms in optical lattices, superconducting circuits, trapped ions and Rydberg atoms [13–15], with different proposals addressing specifically the decay of the false vacuum [16–22]. Two main approaches to quantum simulation involve either using quantum gates on a digital quantum computer to directly emulate the quantum field theory in question, or setting up an analogous system that exhibits a controllable first-order quantum phase transition, where it is possible to initialize in the false vacuum. In this paper, we take the latter approach and set up a quantum annealer with 5564 superconducting flux qubits, which had previously been used to study the spin glass transition [23] and the Kibble-Zurek mechanism [24–26]. We arrange the qubits in a ring by coupling them via ferromagnetic interactions in the presence of a transverse magnetic field, thus realizing the quantum Ising model. By then tuning the uniform longitudinal field, we initialize the system in the metastable false vacuum state and observe the decay into the true vacuum. The discrete nature of the qubit lattice gives us a direct window into the quantized bubble creation, whereby a cascade of bubble sizes is seen to emerge by tuning the longitudinal field. Moreover, the longitudinal field in the

* j.vodeb@fz-juelich.de

† jean-yves.desaulles@ist.ac.at

‡ z.papic@leeds.ac.uk

quantum annealer exhibits intrinsic modulation throughout the decay, driving the dynamics and extending the regime where we observe the same scaling laws as in coherent quantum dynamics up to 1000 qubit time units.

Quench dynamics of the Ising chain in transverse and longitudinal fields have recently attracted much interest due to the confinement effect imposed by the longitudinal field [27–31]. The latter has direct implications for false vacuum decay enabling analytic predictions of the decay rate [32, 33]. Our simulation targets a different regime where quantized bubbles dominate the out-of-equilibrium dynamics, originally proposed in the context of the generalized Kibble-Zurek effect [34]. This enables us to access false vacuum decay dynamics beyond the initial bubble creation and into the previously unexplored regime of interacting bubbles. In contrast to the typical false vacuum decay mechanism [1, 9, 33], we find that a large quantized bubble cannot spread in isolation. It is only through the interaction of two neighboring bubbles that one bubble can enlarge itself by reducing the size of the other. Once reduced to the smallest size of one lattice site, the bubble can then move freely along the system. These results suggest a new physical picture of the false vacuum dynamics as a heterogeneous gas of bubbles, where the smallest “light” bubbles bounce around in the background of larger “heavy” bubbles that directly interact with each other.

I. QUANTUM SIMULATION OF FALSE VACUUM DECAY

We study the ferromagnetic quantum Ising model in transverse and longitudinal fields on a ring with N sites:

$$\hat{H} = -J \sum_{j=1}^N \hat{\sigma}_j^z \hat{\sigma}_{j+1}^z - h_x \sum_{j=1}^N \hat{\sigma}_j^x - h_z \sum_{j=1}^N \hat{\sigma}_j^z, \quad (1)$$

where $\hat{\sigma}^\alpha$ are the Pauli matrices, $J > 0$ is the ferromagnetic interaction strength between nearest-neighbor spins, h_x and h_z are the transverse and longitudinal fields, respectively. We apply periodic boundary conditions by identifying spin $\hat{\sigma}_{N+1}^z \equiv \hat{\sigma}_1^z$. The field h_x drives the quantum dynamics of the system, while h_z imposes an energy bias between the states $|\uparrow\rangle$ and $|\downarrow\rangle$.

In the regime $0 \leq h_x \ll J$ and $h_z = 0$, there are two degenerate ground states $|\uparrow \dots \uparrow\rangle$ and $|\downarrow \dots \downarrow\rangle$. When $h_z > 0$, the $|\uparrow \dots \uparrow\rangle$ state becomes the ground or true vacuum state and $|\downarrow \dots \downarrow\rangle$ a metastable or false vacuum state, see Fig. 1a. By first setting $h_z > 0$ and adiabatically turning on h_x to a small value $h_x \ll J$, we initialize the system in the $|\uparrow \dots \uparrow\rangle$ product state. Then we induce a first-order quantum phase transition by flipping the sign of h_z , swapping the true and false vacuum states, and observe the dynamics for a time duration t . Finally, we turn h_x back to zero as fast as possible and measure the spin configuration in the $\hat{\sigma}^z$ basis. Fig. 1b illustrates the described protocol, while Fig. 1c shows the embedding of the spin chain in a qubit array used in our quantum simulations. We note here that $h_z(t)$ was determined experimentally through single-qubit measurements and exhibits large modulation around the final target value after the flip. This modulation extends up to $t \sim 0.75\mu\text{s}$ in the evolution time and it will play an important role in the interpretation of our data.

Our quantum simulations are performed in the small $h_x \ll J$ regime, where we can apply semiclassical intuition based on the diagonal part of the Hamiltonian in the z -basis. In this case, it is useful to gather possible configurations of the system into sectors with the same value of magnetization, $M = \langle \sum_i \hat{\sigma}_i^z / N \rangle$, separated by energy gaps determined by the value of h_z . For general values of h_z , the initial $|\uparrow \dots \uparrow\rangle$ state stays an eigenstate in its own M -sector after the h_z sign flip and no dynamics of M are observed. This is due to the large energy separation between different M sectors that cannot be hybridized by a small h_x . However, for specific values of $h_z = -2J/n$, where $n > 0$ is an integer, the surface energy cost for flipping a domain of n spins, $4J$, is exactly balanced out by the volume energy gain, $2h_z n$ [34]. Hence, an arbitrarily small h_x is sufficient to hybridize the classical computational basis states into eigenstates consisting of a superposition of the $|\uparrow \dots \uparrow\rangle$ state and so-called n -bubbles, i.e., domain walls in the background of $|\uparrow \dots \uparrow\rangle$. For example, $|\uparrow\uparrow\uparrow\downarrow\downarrow\uparrow\uparrow\rangle$ is a state with a single 3-bubble. Fig. 1d shows the spin configurations measured in our quantum simulations with bubble sizes up to 306 spins, which is consistent with the theoretical prediction in which we can form increasingly larger bubbles by decreasing h_z according to $h_z = -2J/n$. For these discrete values of h_z , the initial state is no longer an eigenstate and undergoes nontrivial quantum dynamics, resulting in large changes in M . Fig. 1e shows the observed $n = 1$ and $n = 2$ resonances, where large changes in M can be seen at $h_z = -2J$ and $h_z = -J$, respectively, in contrast to other values of h_z .

We note that significant changes in M can also be observed in Fig. 1e at values of $h_z \approx -4J$, where no dynamical resonances are expected. Such a large magnitude of h_z leads to thermally assisted adiabatic dynamics [36], where the system can follow the instantaneous ground state during time evolution. The adiabatic theorem is applicable if the time scale of Hamiltonian changes is slower than or comparable to $t_a \propto \Delta_{min}^{-2}$, where Δ_{min} is the minimum gap between the instantaneous ground and first excited state. In the case $|h_z| \gg J, h_x$, the gap becomes large enough for the time scale of $h_z(t)$ to match t_a . Therefore, no bubble creation takes place and the spins turn simultaneously

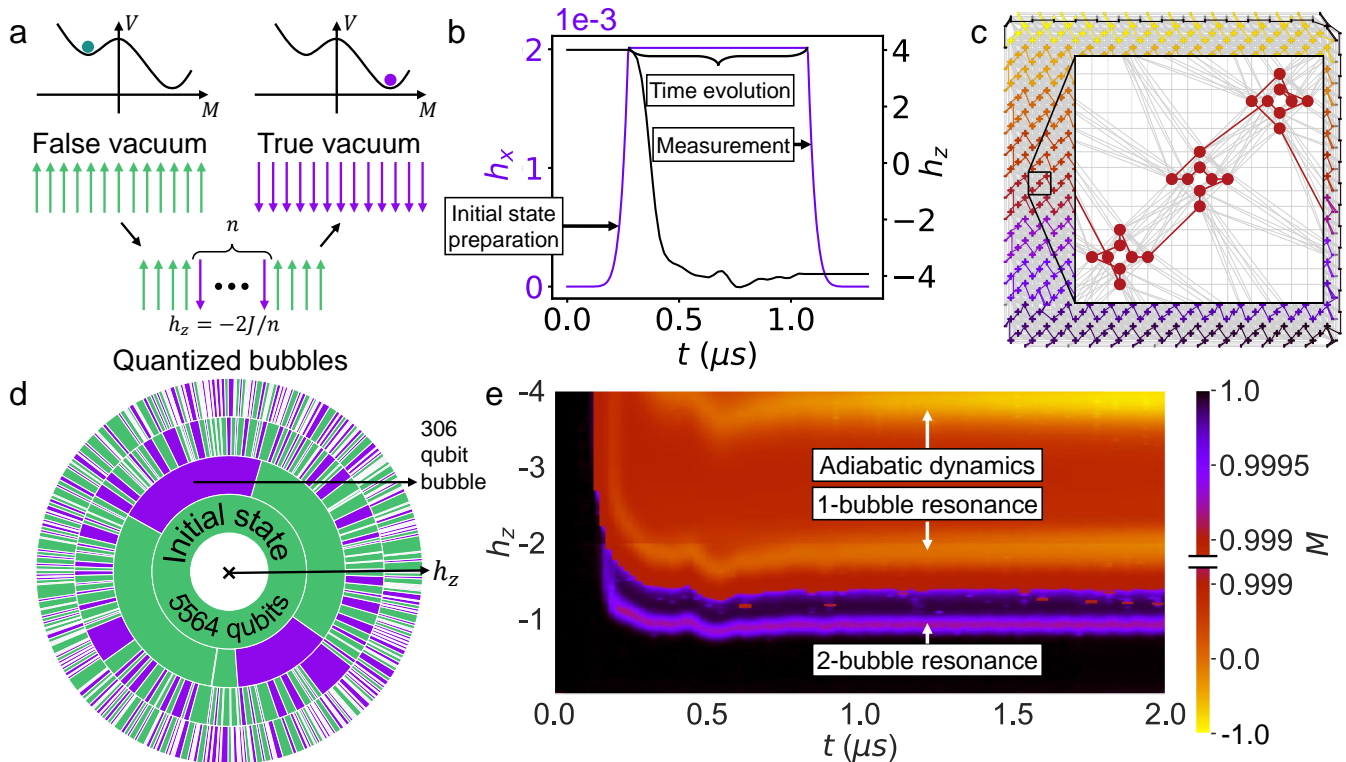


FIG. 1. **Realizing false vacuum decay on a quantum annealer.** **a** The semi-classical energy landscape V as a function of magnetization M of a ferromagnetic Ising chain in a transverse h_x and longitudinal h_z field. The landscape exhibits a local metastable minimum dubbed as the false vacuum, represented by the polarized $|\uparrow\uparrow\cdots\uparrow\rangle$ state. The global minimum or true vacuum is the other polarized $|\downarrow\downarrow\cdots\downarrow\rangle$ state. The false vacuum decay unfolds via creation of quantized true-vacuum bubbles of size n , determined by the energy balance between the surface ($4J$) and volume energy contributions ($2h_z n$). **b** False vacuum decay observation protocol. We initialize all qubits in the $|\uparrow\uparrow\cdots\uparrow\rangle$ state by setting $h_z > 0$ and adiabatically switch h_x from 0 to a small value $h_x \ll J$ over $10\mu s$ ($0.27\mu s$ is used in the plot for clarity purposes). Then we flip the sign of h_z , swapping the true and false vacuum states, and observing the dynamics for a time duration t . Finally, we turn h_x back to 0 as fast as possible ($\geq 0.18\mu s$) and measure the spin configuration in the $\hat{\sigma}^z$ basis. This protocol is repeated 1000 times for each value of t . **c** Embedding of a 5564-qubit ring on the Pegasus graph of the 5614-qubit device D-Wave *Advantage_system5.4*. The Pegasus graph contains $15 \times 15 \times 3$ 8-qubit Chimera cells with complete bipartite connectivity (colored crosses) that are coupled by additional external and odd couplers (gray lines) [35], such that each qubit is connected to 15 other qubits on average. Qubits within the 8-qubit cells are connected along randomly sampled one-dimensional chains (inset). **d** Spin configurations measured in our quantum simulation. The inner ring shows the initial false vacuum state comprised of 5564 spins (for clarity, only 1000 out of 5564 spins in a single configuration are shown). The outer 3 rings show configurations measured at $h_z = -0.1, -0.5, -2$ with h_z decreasing radially. An example of a large $n = 306$ quantized bubble shown in purple highlights the extent of the observed bubble sizes. **e** Magnetization M heat profile versus time t and longitudinal field magnitude h_z at transverse field strength $h_x = 0.002$. The color scheme is split into two separate linear scales, a larger scale from -1 to 0.999 (bottom half) and a smaller scale from 0.999 to 1 (upper half). The adiabatic dynamics and the $n = 1$ -bubble resonance are easily observed on the larger scale, while the $n = 2$ -bubble resonance can only be resolved in the 4th decimal of M , due to the decrease of the rate of dynamics by an order of magnitude. The apparent resonance at $h_z = -4$ is identified with adiabatic dynamics rather than bubble creation, where the system follows an instantaneous ground state during the evolution.

and in accordance with $h_z(t)$ initially, changing the state from fully polarized and triggering more complex resonant processes, see Supplementary Section 2.

II. OBSERVATION OF QUANTIZED BUBBLES AND DYNAMICAL SCALING LAWS

To ascertain which bubbles are involved in magnetization changes, we measured the n -bubble density $\lambda_n = (1/N) \sum_{i=1}^N \langle \hat{P}_i^\uparrow [\prod_{j=1}^n \hat{P}_{i+j}^\downarrow] \hat{P}_{i+n+1}^\uparrow \rangle$, where $\hat{P}^\sigma = |\sigma\rangle\langle\sigma|$ is a projector on the local $\sigma = \uparrow, \downarrow$ spin state. Figures 2a-d show the detected $n = 1, 2, 3, 4, 5, 6$ -bubble resonances. We observe a strong suppression of all other bubble sizes

except the expected ones. According to the theoretical analysis presented in Methods, the leading-order effective Hamiltonian describing an n -bubble resonance is proportional to h_x^n . If we assume $h_x < J$, 1-bubbles are the fastest, then 2-bubbles, etc., arbitrarily slowing down the dynamics as n increases. Figures 2a-d show that we need to increase h_x by at least two orders of magnitude to begin to observe hints of higher resonances through low-density bubble formation, which is consistent with the theoretical prediction.

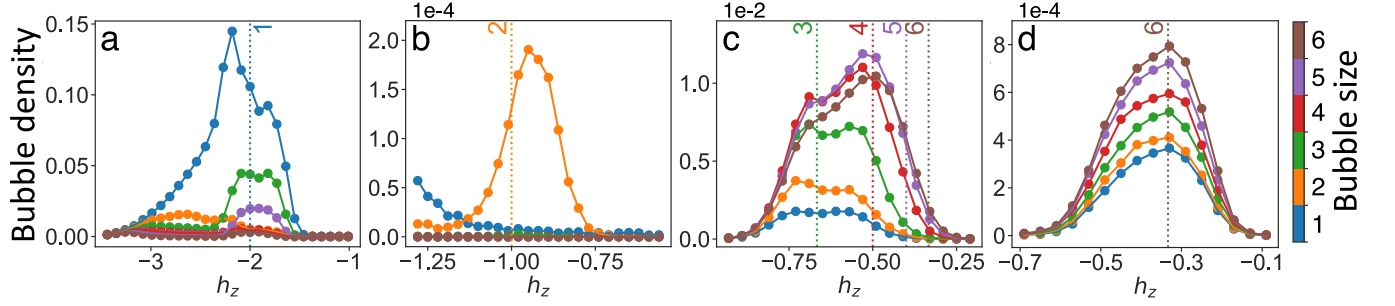


FIG. 2. **Observation of quantized bubbles.** a-d Bubble density measurements at $J = 1$ and different h_z magnitudes, with $h_x = 0.002$, $t = 2\mu\text{s}$ in a,b, $h_x = 0.05$, $t = 1\mu\text{s}$ in c, and $h_x = 0.1$, $t = 1\mu\text{s}$ in d. The bubble sizes $n = 1, 2, \dots, 6$ are seen to be dominant around their respective resonances $h_z = -2J/n$, indicated by vertical dotted lines. Error bars across the entire figure are smaller than the size of the symbols.

In a two-level approximation [34], tunneling events to different n -bubbles can be thought of as Landau-Zener transitions, where the metastable state $|\uparrow \dots \uparrow\rangle$ and an n -bubble state at the appropriate resonant conditions are the two states involved in the anticrossing. According to Landau-Zener theory, it follows that n -bubble density $\lambda_n \propto \tau_Q h_x^n$ should be proportional to the product of the time it takes for the Hamiltonian to traverse the anticrossing τ_Q , determined by $h_z(t)$ in our case, and the n -th power of h_x . Using our single-qubit measurements we show that the time it takes for $h_z(t)$ to reach zero during its sign flip is proportional to the square of its magnitude ($\tau_Q \propto |h_z|^2$), see Supplementary Section 3 for details. This means that $\lambda_n(t)$ curves measured at different pause times between the initialization and measurement ramp t should collapse onto a single curve if we multiply t by h_z^2 . Figure 3a shows that the λ_2 curves indeed exhibit a collapse according to this law.

Nevertheless, in order to fully understand the dynamics in our quantum annealer, it is necessary to account for all dominant processes and not only the creation of bubbles. We will focus on the dynamics from the initial state $|\uparrow \dots \uparrow\rangle$, for which the creation of n -bubbles happens at $h_z = -2J/n$. For each resonance, we have derived the corresponding effective model using the Schrieffer-Wolff transformation [37] and we present the effective Hamiltonians at leading orders in the Methods section. The effective Hamiltonian describing the dynamics at the 2-bubble resonance at $h_z = -J$ is proportional to h_x^2 . Figure 3b shows magnetization measurements taken at this resonance using the quantum annealer and how the $M(t)$ curves collapse when scaling the time axis with h_x^2 . Our numerical emulation

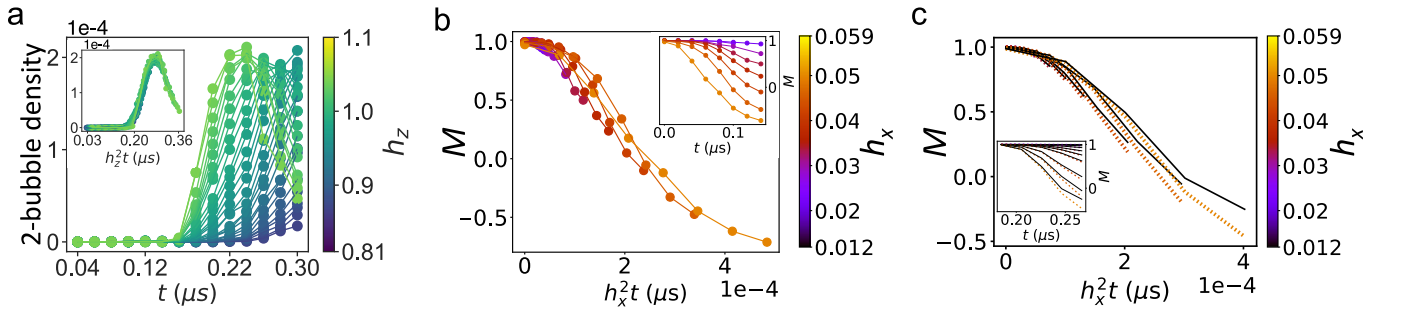


FIG. 3. **Scaling laws for bubble dynamics.** a 2-bubble density at $h_x = 0.002$ as a function of time at various h_z magnitudes (color bar). Inset shows the collapse of different curves when time is rescaled by h_z^2 in accordance with Landau-Zener theory [34]. b-c Magnetization at $h_z = -J$ resonance as a function of rescaled time $h_x^2 t$, for different values of h_x indicated on the color bar. Both the measured magnetization curves in b and the 3-spin Bloch-Redfield numerical simulations in c follow the same h_x^2 scaling law, suggesting that the effective Hamiltonian governing the dynamics is proportional to h_x^2 . The inset in b shows the raw data obtained on the quantum annealer without rescaling. The unscaled results of the numerical simulations are shown in the inset of c, where the black curves show the magnetization in the effective model describing the $h_z = -J$ resonance (see Methods). Error bars across the entire figure are smaller than the size of the symbols.

of the quantum annealer in Fig. 3c suggests that the h_x^2 scaling law is the same as in the case of coherent quantum dynamics. Figure 3b shows only the initial behavior of $M(t)$, which follows the $h_z(t)$ modulation at later times; however, after the $h_z(t)$ modulation stops, an h_x^3 scaling law emerges as a consequence of thermalization combined with a relatively slow quantum simulation ramp, see Supplementary Sections 6-9 for more details.

III. BUBBLE INTERACTIONS

The measured dynamics of different bubble sizes at $h_z = -2J$ resonance in Fig. 4a is consistent with the picture that 1-bubbles remain approximately quantized and do not grow with time. On the quantum annealer, this persists until thermalization kicks in and 1-bubbles start to transform into 3- and 5-bubbles, with 2- and 4-bubbles remaining suppressed throughout the time evolution. The exploration of this peculiar thermalization effect is beyond the scope of this work, as thermalization and bubble interaction effects cannot be easily separated from each other in our quantum annealer due to decoherence effects. Nevertheless, we now argue that bubble interactions play a crucial role in the dynamics at higher $n > 1$ resonances if a system is perfectly isolated from the environment. We will demonstrate this in the framework of effective models, presented in Methods and previously mentioned in the context of Fig. 3.

At the $n = 1$ resonance, 1-bubbles can be created with a rate proportional to h_x . These 1-bubbles can then hop

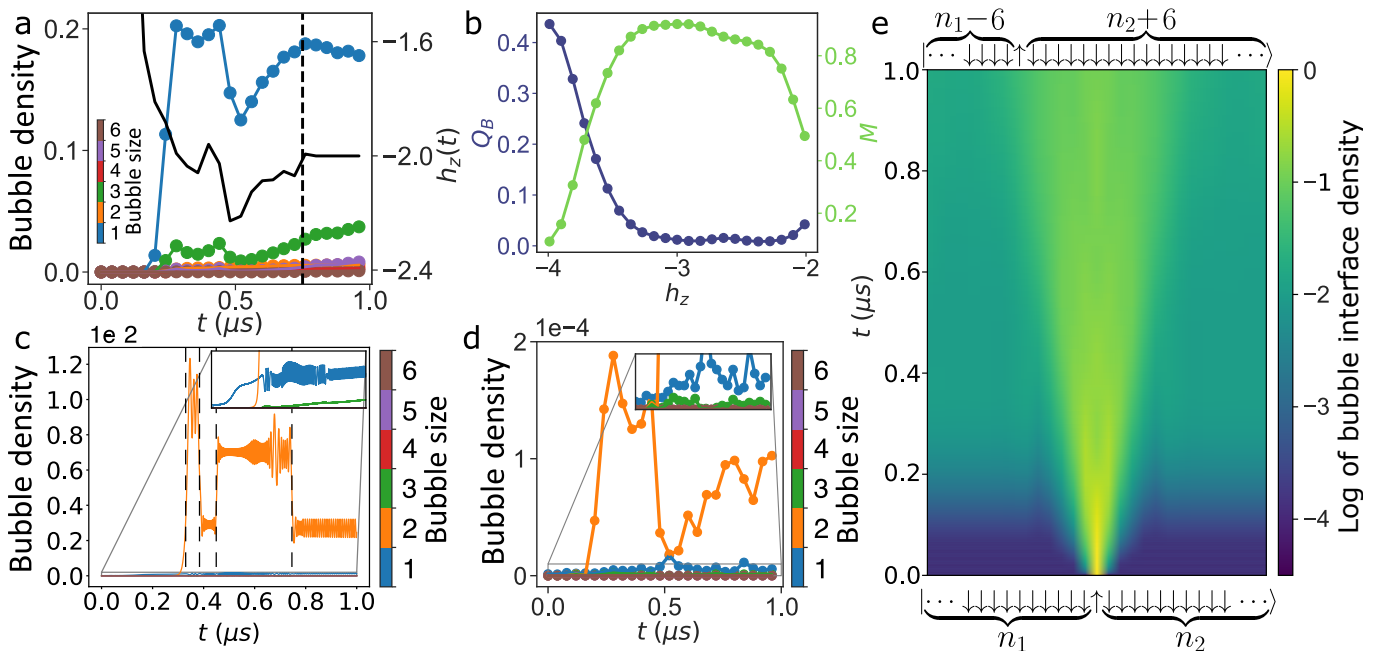


FIG. 4. **a** Time series measurements of the bubble density at the 1-bubble resonance $h_z = -2J$ and $h_x = 0.002$. During the initial $h_z(t)$ modulation, the profile of which is shown by the black curve on the right axis, the 1-bubble density (color bar) governs the dynamics. After about $\sim 0.75 \mu\text{s}$ (dashed line), thermalization effects take over by transforming 1-bubbles into 3- and 5-bubbles. **b** Measurement of the emergent blockade Q_B and magnetization M (right axis) at $h_x = 0.002$ and $t = 0.38 \mu\text{s}$, plotted as a function of h_z magnitude. The blockade condition is violated (deviates from 0) only at h_z values significantly off the 1-bubble resonance ($h_z \leq -3.5$), accompanied by large changes in M . Near the resonance ($h_z \approx -2$), even though large changes in M occur, the blockade condition is respected. **c-d** Dynamics at the resonance $h_z = -J$ with fixed $h_x = 0.0203$ and $h_x = 0.002$, respectively. Matrix-product state simulation with 100 qubits in **c** captures some of the key aspects of the data obtained on the quantum annealer in **d**. The black dashed lines in **c** show the sudden change in the number of 2-bubbles when $h_z(t)$ is exactly at the resonance point. The inset magnifies the low-density regime, where only 1- and 3-bubbles can be seen. The increase of 1- and 3-bubbles at later times is likely due to 2-bubbles interacting. The quantum simulation using $h_x = 0.002$ in **d** shows good agreement with the theoretical prediction in **c**. For all the measured data, error bars are smaller than the symbol size. **e** Matrix-product-state simulation of the dynamics after an instantaneous quench from a product state shown at the bottom, containing two large bubbles ($n_1 = 23$ and $n_2 = 24$ spins) next to each other in a system with 50 spins in total. The system undergoes coherent evolution with fixed $h_z = -1$ and $h_x = 0.02$, and the color bar shows the “bubble interface density”, $\langle \hat{P}_{j-1}^\downarrow \hat{P}_j^\uparrow \hat{P}_{j+1}^\downarrow \rangle$, on a log scale and for all sites j . The moving front corresponds to the two bubbles exchanging \downarrow -spins and changing their sizes. The final state at the end of the evolution is a quantum superposition, with one of the classical configurations shown at the top.

along the chain with a rate proportional to h_x^2/J , but they cannot merge with each other to create large bubbles. In fact, even when accounting for higher-order processes, there is still no path to create $(n > 1)$ -bubbles when starting from the $|\uparrow\uparrow\cdots\rangle$ state. This dictates that, at the $n = 1$ resonance, there can never be two \downarrow -spins next to each other. The system therefore experiences an emergent kinetic constraint, reminiscent of the Rydberg blockade phenomenon [38]. We quantify the blockade by measuring the operator $\hat{Q}_B = (1/N) \sum_j \hat{P}_j^\downarrow \hat{P}_{j+1}^\downarrow$, which counts the density of neighboring \downarrow -spins. We expect $\langle \hat{Q}_B \rangle$ to be strongly suppressed around $h_z = -2J$, rising towards 0.5 in other dynamical settings. Figure 4b shows a good match between these predictions and quantum simulation data. Meanwhile, total magnetization strongly deviates from the initial value of 1, showing that the lack of neighboring excitations is not trivially due to frozen dynamics.

Now we consider higher-order resonances $h_z = -2J/n$, with $n > 1$, where bubbles contain n spins and are created at a rate proportional to h_x^n/J^{n-1} . Once these large bubbles are created, they cannot hop around. However, bubbles can now take or give \downarrow -spins to neighboring bubbles, allowing them to change size. This occurs with a rate $\propto h_x^2/J$ which, for large n , is much faster than bubble creation. This can also lead to a bubble shrinking all the way down to a 1-bubble, which can then hop along the chain. This means that, despite large bubbles being stuck in place, information can still flow through inter-bubble interactions and movement of 1-bubbles.

Our theoretical predictions imply that, in a quantum simulation tuned to a $n > 1$ resonance, the size of bubbles is not limited to n , even if the system is perfectly isolated from the environment. This can be seen in a fully coherent matrix-product state simulation of a system with $N = 100$ spins at $n = 2$ resonance in Fig. 4c. While 2-bubbles dominate, 1- and 3-bubbles are also visible. This is expected as they are produced by interactions of 2-bubbles. Qualitatively similar behavior is also seen in the quantum simulation data in Fig. 4d.

The data in Figs. 4c-d also highlights another important property for $n > 1$: the number of 2-bubbles changes abruptly at some times, while staying approximately constant during the rest of the simulation. The timings of abrupt changes coincide exactly with $h_z(t)$ hitting the appropriate resonant value, while the rest of the time the system is slightly away from the resonance. This highlights the sensitivity to the detuning, $\delta = h_z + 2J/n$, which competes with h_x^n/J^{n-1} . As $h_x/J \ll 1$, even a small δ is enough to overpower the bubble creation terms for $n > 1$. As the detuning is a diagonal contribution, it leads to the suppression of all dynamical processes, including bubble creation. This pattern of sudden changes due to the fluctuation of h_z is clearly captured in the numerical simulation in Fig. 4c but it is also visible in the annealer data in Fig. 4d. We note that this sensitivity to detuning is expected to be less strong for $n = 1$, as in that case δ only competes with h_x .

To further highlight the importance of bubble interactions, we have studied a closed system with two large bubbles next to each other and essentially occupying the entire system, see Fig. 4e. This setup leaves no room for new bubbles to appear, and the only resonant process left is the exchange between the two bubbles. We can then track the interface between them by measuring $\hat{P}_{j-1}^\downarrow \hat{P}_j^\uparrow \hat{P}_{j+1}^\downarrow$, which is plotted on a log scale in Fig. 4e at the $h_z = -J$ resonance. While the interface density is 1 at a single location at time $t = 0$ and zero everywhere else, as time goes on the interface steadily delocalizes due to the bubbles exchanging \downarrow -spins and thereby changing their sizes. We expect similar behavior to hold at other $n > 1$ resonances.

IV. DISCUSSION AND OUTLOOK

We have performed a quantum simulation of the false vacuum decay and identified its underlying mechanism – the formation of quantized bubbles of true vacuum. The large size of our 5564-qubit quantum annealer allowed us to observe considerable bubble sizes comprising up to 300 spin flips, confirming the standard cosmological scenario where the size of the formed bubble is determined by the competition between the volume energy gain and surface energy loss. Our central finding is that interactions between bubbles are the key next-order effect after bubble creation, and we have argued that their understanding is crucial for a comprehensive description of false vacuum decay. Previous studies of false vacuum decay in quantum spin chains [32, 33] have explored a different parameter regime where h_x is not small and the energy spectrum forms a continuum. While the possibility of resonances was pointed out as a subleading effect [32], these analytical considerations still assume a dilute bubble picture, neglecting interactions between bubbles. Our results therefore call for a deeper understanding of the interaction effects between bubbles, not only in microscopic models such as the one studied here, but also in quantum field theory approaches, including cosmological models of the Big Bang.

More broadly, our work showcases that current quantum annealing devices can be useful in probing complex many-body dynamics, e.g., as demonstrated here through external field modulation on a scale of 1000 individual qubit time units. Extensions of our model to two or three spatial dimensions with various lattice topologies are, in principle, straightforward on the same type of device, potentially reaching intractable computational complexity with a multitude of implications. Let us mention a few examples of other interesting non-equilibrium phenomena that can be accessed in the platform established here. False vacuum decay, as a specific instance of a first-order quantum

phase transition, allows to probe generalizations of the Kibble-Zurek scaling laws [11, 39–41] in such transitions, in particular comparing the predictions for the rate of defect formation after crossing the transition with quantum simulations. Quantum metastability – the cornerstone of the false vacuum decay phenomenon – also underlies reaction rate theory [42–47], allowing the use of quantum simulation for estimating the transition rate of decay processes from a metastable minimum to a lower energy state in the presence of temperature, which is challenging to compute otherwise. In the regime of stronger longitudinal fields, confinement effects are expected to become important, possibly localizing bubbles in space and giving rise to an emergent prethermalization regime [48]. Finally, at the 1-bubble resonance, our model displays an emergent kinetic constraint that maps exactly to the so-called PXP model [49, 50] (see Methods), which hosts quantum many-body scars [38, 51, 52], and possibly other types of ergodicity breaking, such as Hilbert space fragmentation and many-body localization, in higher dimensions [53, 54]. This opens the way to probing non-ergodic phenomena in large systems in the presence of dissipation and potentially new types of scars in constrained models at other $n > 1$ resonances.

V. METHODS

A. Quantum simulation on D-Wave’s quantum annealer

Our quantum simulations utilized D-Wave’s quantum annealing device *Advantage_system5.4*, which features $N_q = 5614$ qubits and is kept at a cryostat temperature of 16.4 ± 0.1 mK. The annealer implements the Hamiltonian

$$\hat{H}_{\text{DW}} = -\frac{A(s)}{2} \left(\sum_{i=1}^{N_q} \hat{\sigma}_i^x \right) + \frac{B(s)}{2} \left(g(t) \sum_{i=1}^{N_q} h_i \hat{\sigma}_i^z + \sum_{i < j}^{N_q} J_{ij} \hat{\sigma}_i^z \hat{\sigma}_j^z \right), \quad (2)$$

where $\hat{\sigma}_i^{x,z}$ are the Pauli matrices for the i th qubit, h_i is the longitudinal external field at qubit i , J_{ij} are the couplings between qubits i and j , which are non-zero and user-tunable only if they are physically connected in the quantum processing unit (Fig. 1c). $A(s)$ and $B(s)$ represent the energy scales of their respective terms and are driven in time by the annealing schedule $s(t)$, which is linearly interpolated from a series of user-specified points $[(t_i, s_i)]$.

Finding a ring embedding in a given graph is an instance of an NP-complete Hamiltonian circuit problem [55]. We generate our ring embedding on 5564 qubits of the *Advantage_system5.4* graph by first connecting all 8-qubit Chimera cells in the Pegasus topology, see Fig. 1c. We start in the upper-left corner and proceed horizontally, changing the horizontal direction at the end of every row, until we reach the bottom-right corner. The chain of qubits within each 8-qubit Chimera cell is chosen along a random suitable path, see Fig. 1c inset. The ring is closed by proceeding along the outer qubits at the right and top edge of the graph (black part of the chain in Fig. 1c). This procedure yields a ring of 5446 qubits. We then iteratively add qubits to the chain from the set of omitted remaining qubits by adding detours into the ring until we obtain the final 5564-qubit closed chain. We note that a few of the qubits and couplers in the full Pegasus graph are not present on the device due to fabrication defects; these are accounted for individually.

We are interested in probing the dynamics of \hat{H} in Eq. (1) at a certain value of h_x . Therefore, we specify the annealing schedule as $[(0, 1), (irt, s_{h_x}), (irt + pt, s_{h_x}), (irt + pt + mt, 1)]$, where s_{h_x} is obtained from the relation $h_x = A(s_{h_x})/B(s_{h_x})$, obtained by rewriting \hat{H}_{DW} as $(B(s)/2)\hat{H}$. We choose uniform $h_i = h$, $J_{ij} = -1$ and define $h_x = A(s)/B(s)$, $h_z = -g(t)h$. At time $t = 0$, we specify the initial state for all qubits as the product state $|\uparrow \dots \uparrow\rangle$. Then, within the initial ramp time irt , we bring the system to the desired h_x value, which drives the dynamics we are interested in, and keep it constant for time pt . We replace pt with t in all plots. Finally, we bring h_x to 0 within time mt , which constitutes a measurement. Only after h_x is brought back to 0 is it possible to read out the state of the qubits in the computational or $\hat{\sigma}^z$ basis.

Typical time scales that we used on the D-Wave device are $irt = 10\mu\text{s}$, $mt = 272\text{ns}$, and pt ranging from 0 to $2\mu\text{s}$. After the initial state preparation, the system remains in the $|\uparrow \dots \uparrow\rangle$ state due to the small values of h_x compared to h_z . During the entire time evolution, which lasts for a time $irt + pt + mt$, the system is subject to open system dynamics, governed by two main effects; measurement by the environment and thermalization. Our single spin measurements show that measurement by the environment is dominant whenever the system is being driven by the longitudinal external field h_z . Whenever h_z becomes constant, thermalization effects become more evident and are heavily dependent on the value of h_x , which drives the quantum dynamics of the system – see Supplementary Sections 7 and 9.

B. Simulations of thermalization dynamics

To capture thermalization effects on the system's dynamics, we employed the Bloch-Redfield master equation [56]

$$\frac{d}{dt}\rho_{ab}(t) = -i\omega_{ab}\rho_{ab}(t) + \sum_{cd}^{sec} R_{abcd}\rho_{cd}, \quad (3)$$

where $\hat{\rho}$ is the density matrix of the system, $\omega_{ab} \equiv \omega_a - \omega_b$ with $\omega_a = E_a/\hbar$ and E_a being the eigenenergies of the system. *sec* denotes the secular approximation, which states that we can neglect all fast-rotating terms in the sum, and R_{abcd} is the Bloch-Redfield tensor [56]

$$R_{abcd} = -\frac{1}{2\hbar^2} \sum_{\alpha,\beta} \left\{ \delta_{bd} \sum_n A_{an}^\alpha A_{nc}^\beta S_{\alpha\beta}(\omega_{cn}) - A_{ac}^\alpha A_{db}^\beta S_{\alpha\beta}(\omega_{ca}) + \delta_{ac} \sum_n A_{dn}^\alpha A_{nb}^\beta S_{\alpha\beta}(\omega_{dn}) - A_{ac}^\alpha A_{db}^\beta S_{\alpha\beta}(\omega_{db}) \right\}, \quad (4)$$

where A_{ab}^α are the matrix elements in the system's eigenbasis of the operator A^α that couples bilinearly to the bath. Here we choose $A^\alpha = \sigma_\alpha^z$, where α runs through all the spins of the system. $S_{\alpha\beta}(\omega) = \eta\omega\theta(\omega) \exp(\omega/\omega_c)$ is the noise power spectrum of the bath, chosen to be Ohmic in our case, where $\theta(\omega)$ is the Heaviside step function, η the coupling strength of the system-bath coupling that ranges from 0.1 to 0.2 in our case, and ω_c a cutoff frequency higher than any other relevant energy scale.

The numerical simulations in Figs. 4c,e were performed under the assumption of a closed system using matrix-product state (MPS) formalism [57]. For efficiency, the simulated system has open boundary conditions, but we discard the boundary sites when computing observable expectation values in order to minimize boundary effects. To reach the long times required for the simulation, a 4th-order time-evolving block decimation (TEBD4) was used [58, 59]. For Fig. 4c, the timestep is $\delta t = 0.01$ while the maximum MPS bond dimension is $\chi = 128$, which was never saturated during the simulation. For Fig. 4e, the timestep is $t=0.05$ while the maximum bond dimension is $\chi = 200$.

C. Effective models at different resonances

To fully understand the dynamics beyond bubble creation in the vicinity of resonances, we have derived the corresponding effective Hamiltonians using the Schrieffer-Wolff transformation [37]. We quote the main results here, while the derivation and detailed analysis of the models are provided in Supplementary Section 5. For $n = 1$, in the sector containing the state $|\uparrow \cdots \uparrow\rangle$, the combined effective Hamiltonian at first and second order reads:

$$\hat{H}_{\text{eff},n=1}^{(1,2)} = -h_x \sum_{j=1}^N \hat{P}_{j-1}^\uparrow \hat{\sigma}_j^x \hat{P}_{j+1}^\uparrow - \delta \sum_{j=1}^N \hat{\sigma}_j^z + \frac{h_x^2}{4J} \left[\sum_{j=1}^N \hat{P}_{j-1}^\uparrow (\hat{\sigma}_j^+ \hat{\sigma}_{j+1}^- + \hat{\sigma}_j^- \hat{\sigma}_{j+1}^+) \hat{P}_{j+2}^\uparrow + 2 \sum_{j=1}^N \hat{P}_j^\downarrow - \frac{3}{2} \sum_{j=1}^N \hat{P}_{j-1}^\downarrow \hat{P}_{j+1}^\downarrow \right], \quad (5)$$

where $\delta = h_z + 2J$ is the (weak) detuning away from the $n = 1$ resonance, $\hat{\sigma}^\pm = (\hat{\sigma}^x \pm i\hat{\sigma}^y)/2$ are the standard spin raising and lowering operators, and $\hat{P}^\downarrow = |\downarrow\rangle\langle\downarrow|$, $\hat{P}^\uparrow = |\uparrow\rangle\langle\uparrow|$ are local spin projectors.

The dynamics generated by the Hamiltonian in Eq. (5) can be understood as follows. The $\hat{P}^\uparrow \hat{\sigma}^x \hat{P}^\uparrow$ term allows the creation of single-site bubbles (i.e., single \downarrow -spins in a background of \uparrow -spins), while the $\hat{P}^\uparrow (\hat{\sigma}^+ \hat{\sigma}^- + \hat{\sigma}^- \hat{\sigma}^+) \hat{P}^\uparrow$ allows these bubbles to hop around. A sequence of allowed processes is illustrated in Fig. 5. Importantly, due to the projectors, the bubbles cannot merge to form larger ones. This is also impossible to do using higher-order processes. A simple argument is that there are no states with larger bubbles at the same classical energy (i.e., the energy contribution of the $\hat{\sigma}^z$ terms) as the $|\uparrow\uparrow\uparrow \cdots\rangle$ state, so it is impossible to reach these states resonantly.

In the main text, we have demonstrated that one measurable consequence of the effective Hamiltonian in Eq. (5) is a robust emergent kinetic constraint reminiscent of the Rydberg blockade [38]. The quality of this emergent blockade can be assessed using the operator \hat{Q}_B introduced in the main text, which measures the density of neighboring \downarrow -spins and can be equivalently expressed in the spin language as $\hat{Q}_B = 1/4 + (1/(4N)) \sum_j \hat{\sigma}_j^z \hat{\sigma}_{j+1}^z - (1/(2N)) \sum_j \hat{\sigma}_j^z$.

For $n > 1$ resonances, the bubble creation term is no longer dominant as it happens at order n according to

$$\hat{H}_{\text{eff},n} = c_n \frac{h_x^n}{J^{n-1}} \sum_{j=1}^N \hat{P}_j^\uparrow \left(\prod_{k=1}^n \hat{\sigma}_{j+k}^- \right) \hat{P}_{j+n+1}^\uparrow + \text{h.c.}, \quad (6)$$

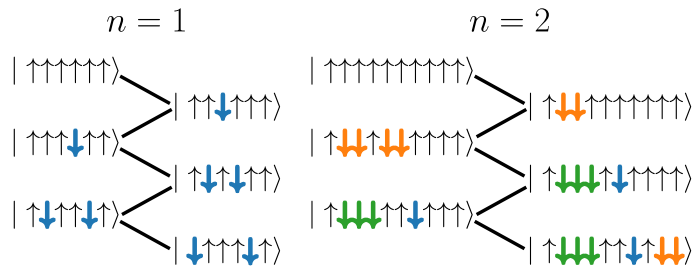


FIG. 5. Schematic of the allowed dynamical processes at $n = 1$ and $n = 2$ resonances. At $n = 1$, the 1-bubbles can be directly created and move along the chain. However, they cannot merge and their size is fixed. By contrast, for $n > 1$ (here illustrated for $n = 2$) only n -bubbles can form. While these larger bubbles cannot move, neighboring bubbles can exchange \downarrow -spins to change their size. If 1-bubbles are formed that way, they can hop along the chain unlike bigger bubbles.

where c_n is a coefficient that depends on the multiple subprocesses involved, e.g., we have $c_2 = -1$ and $c_3 = -81/64$. Instead, regardless of n there are always other terms at order one and two that read

$$\begin{aligned} \hat{H}_{\text{eff},n=2}^{(1,2)} = & -\delta \sum_{j=1}^N \hat{\sigma}_j^z + \frac{h_x^2 n}{4J} \sum_{j=1}^N \left(\frac{\hat{P}_{j-1}^\downarrow \hat{\sigma}_j^z \hat{P}_{j+1}^\downarrow}{n+1} + \hat{P}_{j-1}^\uparrow \hat{\sigma}_j^z \hat{P}_{j+1}^\downarrow + \hat{P}_{j-1}^\downarrow \hat{\sigma}_j^z \hat{P}_{j+1}^\uparrow - \frac{\hat{P}_{j-1}^\uparrow \hat{\sigma}_j^z \hat{P}_{j+1}^\uparrow}{n-1} \right) \\ & + \frac{h_x^2 n^2}{4J(n-1)} \sum_{j=1}^N \hat{P}_{j-1}^\uparrow (\hat{\sigma}_j^+ \hat{\sigma}_{j+1}^- + \hat{\sigma}_j^- \hat{\sigma}_{j+1}^+) \hat{P}_{j+2}^\uparrow - \frac{h_x^2 n^2}{4J(n+1)} \sum_{j=1}^N \hat{P}_{j-1}^\downarrow (\hat{\sigma}_j^+ \hat{\sigma}_{j+1}^- + \hat{\sigma}_j^- \hat{\sigma}_{j+1}^+) \hat{P}_{j+2}^\downarrow. \end{aligned} \quad (7)$$

The terms on the second line create different dynamics. The first one leads to 1-bubbles hopping (as for $n = 1$), while the second one allows larger bubbles to exchange down-spins in order to grow or shrink. This allows bubbles of size other than n to develop. This includes the case of larger bubbles shrinking all the way down to 1-bubble and then moving on their own. A sequence of these allowed processes is illustrated in Fig. 5 for $n = 2$, with higher n values displaying qualitatively similar behaviors. The dynamics at $n > 1$ resonances are clearly much richer than at $n = 1$. Indeed, while the bubble interaction term should also be present for $n = 1$, it cannot act between two 1-bubbles. This would require one of them to shrink to 0, which is not resonant. Thus, in the sector of the $|\uparrow \cdots \uparrow\rangle$ state where only 1-bubbles appear, the bubble interaction term vanishes.

Finally, it is worth noting that the first term of the effective Hamiltonian at the $n = 1$ resonance [Eq. (5)], up to a global spin flip, is identical to the PXP model used to describe chains of Rydberg atoms [49, 50]. The second term can then be recast as $-2\delta \sum_j \hat{P}_j^\downarrow$ up to an irrelevant constant, and then becomes the chemical potential for the effective PXP model. On the other hand, to the best of our knowledge, the effective Hamiltonians for $n > 1$ resonances, Eq. (7), do not map to the models previously studied in the literature.

VI. ACKNOWLEDGEMENTS

J.V., D.W. and M.W. acknowledge support from the project Jülich UNified Infrastructure for Quantum computing (JUNIQ) that has received funding from the German Federal Ministry of Education and Research (BMBF) and the Ministry of Culture and Science of the State of North Rhine-Westphalia. A.R. acknowledges support from the project HPCQS (101018180) of the European High-Performance Computing Joint Undertaking (EuroHPC JU). J.-Y.D., A.H. and Z.P. acknowledge support by the Leverhulme Trust Research Leadership Award RL-2019-015 and EPSRC grants EP/R513258/1, EP/W026848/1. J.-Y.D. acknowledges support from the European Union's Horizon 2020 research and innovation programme under the Marie Skłodowska-Curie Grant Agreement No.101034413. This research was supported in part by grants NSF PHY-1748958 and PHY-2309135 to the Kavli Institute for Theoretical Physics (KITP). Computational portions of this research work were carried out on ARC3 and ARC4, part of the High-Performance Computing facilities at the University of Leeds, UK. G.H. would like to acknowledge the financial support from ARIS, P1-0040 Nonequilibrium Quantum System Dynamics. The authors gratefully acknowledge the Jülich Supercomputing Centre (<https://www.fzjuelich.de/ias/jsc>) for funding this project by providing computing time on the D-Wave Advantage™ System JUPSI through the Jülich UNified Infrastructure for Quantum computing (JUNIQ). We would like to acknowledge the helpful theoretical discussions with Gianluca Lagnese and the quantum simulation related discussions with D-Wave's experimental team, in particular Allison MacDonald, Gabriel Poulin-Lamarre, Axel Daian and Andrew Berkley. We also thank Victoria Goliber and Andy Mason for patiently organizing and mediating the corresponding meetings that enabled the discussions with D-Wave's team.

VII. AUTHOR CONTRIBUTIONS STATEMENT

J.V. conceptualized and performed the quantum simulations. J.V., D.W., F.J. and G.H. designed and analyzed the quantum simulations, whose coherent emulation was performed by A.R. and M.W. J-Y.D., A.H. and Z.P. conducted the theoretical analysis. J.V., J-Y.D., D.W. and Z.P. co-wrote the manuscript with input from other authors. All authors participated in the discussions of the results and development of the manuscript.

VIII. COMPETING INTERESTS STATEMENT

The authors declare no competing interests.

-
- [1] S. Coleman, Fate of the false vacuum: Semiclassical theory, *Phys. Rev. D* **15**, 2929 (1977).
- [2] I. Kobsarev, L. B. Okun, and M. V. Voloshin, *Bubbles in metastable vacuum*, Tech. Rep. (Moscow Institute for Theoretical and Experimental Physics, USSR, 1974) iTEP–81.
- [3] A. Linde, Fate of the false vacuum at finite temperature: Theory and applications, *Physics Letters B* **100**, 37 (1981).
- [4] A. H. Guth, Inflationary universe: A possible solution to the horizon and flatness problems, *Phys. Rev. D* **23**, 347 (1981).
- [5] S. Hawking and I. Moss, Supercooled phase transitions in the very early universe, *Physics Letters B* **110**, 35 (1982).
- [6] E. Abdalla, G. F. Abellán, A. Aboubrahim, A. Agnello, Ö. Akarsu, Y. Akrami, G. Alestas, D. Aloni, L. Amendola, L. A. Anchordoqui, *et al.*, Cosmology intertwined: A review of the particle physics, astrophysics, and cosmology associated with the cosmological tensions and anomalies, *Journal of High Energy Astrophysics* **34**, 49 (2022).
- [7] G. Isidori, G. Ridolfi, and A. Strumia, On the metastability of the Standard Model vacuum, *Nuclear Physics B* **609**, 387 (2001).
- [8] G. Degrassi, S. Di Vita, J. Elias-Miro, J. R. Espinosa, G. F. Giudice, G. Isidori, and A. Strumia, Higgs mass and vacuum stability in the standard model at NNLO, *Journal of High Energy Physics* **2012**, 1 (2012).
- [9] C. Caprini, M. Chala, G. C. Dorsch, M. Hindmarsh, S. J. Huber, T. Konstandin, J. Kozaczuk, G. Nardini, J. M. No, K. Rummukainen, *et al.*, Detecting gravitational waves from cosmological phase transitions with LISA: an update, *Journal of Cosmology and Astroparticle Physics* **2020** (03), 024.
- [10] E. Farhi, A. H. Guth, and J. Guven, Is it possible to create a universe in the laboratory by quantum tunneling?, *Nuclear Physics B* **339**, 417 (1990).
- [11] W. H. Zurek, Cosmological experiments in condensed matter systems, *Physics Reports* **276**, 177 (1996).
- [12] A. Zenesini, A. Berti, R. Cominotti, C. Rogora, I. G. Moss, T. P. Billam, I. Carusotto, G. Lamporesi, A. Recati, and G. Ferrari, False vacuum decay via bubble formation in ferromagnetic superfluids, *Nature Physics* **20**, 558 (2024).
- [13] M. C. Bañuls, R. Blatt, J. Catani, A. Celi, J. I. Cirac, M. Dalmonte, L. Fallani, K. Jansen, M. Lewenstein, S. Montangero, C. A. Muschik, B. Reznik, E. Rico, L. Tagliacozzo, K. Van Acoleyen, F. Verstraete, U.-J. Wiese, M. Wingate, J. Zakrzewski, and P. Zoller, Simulating lattice gauge theories within quantum technologies, *The European Physical Journal D* **74**, 165 (2020).
- [14] C. W. Bauer, Z. Davoudi, A. B. Balantekin, T. Bhattacharya, M. Carena, W. A. de Jong, P. Draper, A. El-Khadra, N. Gemelke, M. Hanada, D. Kharzeev, H. Lamm, Y.-Y. Li, J. Liu, M. Lukin, Y. Meurice, C. Monroe, B. Nachman, G. Pagano, J. Preskill, E. Rinaldi, A. Roggero, D. I. Santiago, M. J. Savage, I. Siddiqi, G. Siopsis, D. Van Zanten, N. Wiebe, Y. Yamauchi, K. Yeter-Aydeniz, and S. Zorzetti, Quantum simulation for high-energy physics, *PRX Quantum* **4**, 027001 (2023).
- [15] J. C. Halimeh, M. Aidelburger, F. Grusdt, P. Hauke, and B. Yang, Cold-atom quantum simulators of gauge theories (2023), [arXiv:2310.12201](https://arxiv.org/abs/2310.12201) [[cond-mat.quant-gas](https://arxiv.org/abs/2310.12201)].
- [16] T. P. Billam, R. Gregory, F. Michel, and I. G. Moss, Simulating seeded vacuum decay in a cold atom system, *Phys. Rev. D* **100**, 065016 (2019).
- [17] T. P. Billam, K. Brown, and I. G. Moss, Simulating cosmological supercooling with a cold-atom system, *Phys. Rev. A* **102**, 043324 (2020).
- [18] S. Abel and M. Spannowsky, Quantum-field-theoretic simulation platform for observing the fate of the false vacuum, *PRX Quantum* **2**, 010349 (2021).
- [19] K. L. Ng, B. Opanchuk, M. Thenabadu, M. Reid, and P. D. Drummond, Fate of the false vacuum: Finite temperature, entropy, and topological phase in quantum simulations of the early universe, *PRX Quantum* **2**, 010350 (2021).
- [20] A. Milsted, J. Liu, J. Preskill, and G. Vidal, Collisions of false-vacuum bubble walls in a quantum spin chain, *PRX Quantum* **3**, 020316 (2022).
- [21] S. Darbha, M. Kornjača, F. Liu, J. Balewski, M. R. Hirsbrunner, P. Lopes, S.-T. Wang, R. V. Beeumen, D. Camps, and K. Klymko, False vacuum decay and nucleation dynamics in neutral atom systems (2024), [arXiv:2404.12360](https://arxiv.org/abs/2404.12360) [[quant-ph](https://arxiv.org/abs/2404.12360)].
- [22] S. Darbha, M. Kornjača, F. Liu, J. Balewski, M. R. Hirsbrunner, P. Lopes, S.-T. Wang, R. V. Beeumen, K. Klymko, and D. Camps, Long-lived oscillations of false and true vacuum states in neutral atom systems (2024), [arXiv:2404.12371](https://arxiv.org/abs/2404.12371) [[quant-ph](https://arxiv.org/abs/2404.12371)].

- [23] R. Harris, Y. Sato, A. J. Berkley, M. Reis, F. Altomare, M. H. Amin, K. Boothby, P. Bunyk, C. Deng, C. Enderud, S. Huang, E. Hoskinson, M. W. Johnson, E. Ladizinsky, N. Ladizinsky, T. Lanting, R. Li, T. Medina, R. Molavi, R. Neufeld, T. Oh, I. Pavlov, I. Perminov, G. Poulin-Lamarre, C. Rich, A. Smirnov, L. Swenson, N. Tsai, M. Volkmann, J. Whittaker, and J. Yao, Phase transitions in a programmable quantum spin glass simulator, *Science* **361**, 162 (2018).
- [24] Y. Bando, Y. Susa, H. Oshiyama, N. Shibata, M. Ohzeki, F. J. Gómez-Ruiz, D. A. Lidar, S. Suzuki, A. del Campo, and H. Nishimori, Probing the universality of topological defect formation in a quantum annealer: Kibble-zurek mechanism and beyond, *Phys. Rev. Res.* **2**, 033369 (2020).
- [25] A. D. King, S. Suzuki, J. Raymond, A. Zucca, T. Lanting, F. Altomare, A. J. Berkley, S. Ejtemaee, E. Hoskinson, S. Huang, E. Ladizinsky, A. J. R. MacDonald, G. Marsden, T. Oh, G. Poulin-Lamarre, M. Reis, C. Rich, Y. Sato, J. D. Whittaker, J. Yao, R. Harris, D. A. Lidar, H. Nishimori, and M. H. Amin, Coherent quantum annealing in a programmable 2,000 qubit ising chain, *Nature Physics* **18**, 1324 (2022).
- [26] A. D. King, J. Raymond, T. Lanting, R. Harris, A. Zucca, F. Altomare, A. J. Berkley, K. Boothby, S. Ejtemaee, C. Enderud, E. Hoskinson, S. Huang, E. Ladizinsky, A. J. R. MacDonald, G. Marsden, R. Molavi, T. Oh, G. Poulin-Lamarre, M. Reis, C. Rich, Y. Sato, N. Tsai, M. Volkmann, J. D. Whittaker, J. Yao, A. W. Sandvik, and M. H. Amin, Quantum critical dynamics in a 5,000-qubit programmable spin glass, *Nature* **617**, 61 (2023).
- [27] M. Kormos, M. Collura, G. Takács, and P. Calabrese, Real-time confinement following a quantum quench to a non-integrable model, *Nat. Phys.* **13**, 246 (2017).
- [28] F. Liu, R. Lundgren, P. Titum, G. Pagano, J. Zhang, C. Monroe, and A. V. Gorshkov, Confined quasiparticle dynamics in long-range interacting quantum spin chains, *Phys. Rev. Lett.* **122**, 150601 (2019).
- [29] W. L. Tan, P. Becker, F. Liu, G. Pagano, K. Collins, A. De, L. Feng, H. Kaplan, A. Kyprianidis, R. Lundgren, *et al.*, Domain-wall confinement and dynamics in a quantum simulator, *Nat. Phys.* **17**, 742 (2021).
- [30] J. Vovrosh and J. Knolle, Confinement and entanglement dynamics on a digital quantum computer, *Scientific reports* **11**, 11577 (2021).
- [31] G. Lagnese, F. M. Surace, S. Morampudi, and F. Wilczek, Detecting a long lived false vacuum with quantum quenches (2023), [arXiv:2308.08340 \[cond-mat.stat-mech\]](https://arxiv.org/abs/2308.08340).
- [32] S. B. Rutkevich, Decay of the metastable phase in $d = 1$ and $d = 2$ ising models, *Phys. Rev. B* **60**, 14525 (1999).
- [33] G. Lagnese, F. M. Surace, M. Kormos, and P. Calabrese, False vacuum decay in quantum spin chains, *Phys. Rev. B* **104**, L201106 (2021).
- [34] A. Sinha, T. Chanda, and J. Dziarmaga, Nonadiabatic dynamics across a first-order quantum phase transition: Quantized bubble nucleation, *Phys. Rev. B* **103**, L220302 (2021).
- [35] D-Wave Systems, *Technical Description of the D-Wave Quantum Processing Unit*, Tech. Rep. (D-Wave Systems Inc., Burnaby, BC, Canada, 2020) D-Wave User Manual 09-1109A-V.
- [36] M. H. S. Amin, P. J. Love, and C. J. S. Truncik, Thermally assisted adiabatic quantum computation, *Phys. Rev. Lett.* **100**, 060503 (2008).
- [37] S. Bravyi, D. P. DiVincenzo, and D. Loss, Schrieffer-wolff transformation for quantum many-body systems, *Annals of Physics* **326**, 2793 (2011).
- [38] H. Bernien, S. Schwartz, A. Keesling, H. Levine, A. Omran, H. Pichler, S. Choi, A. S. Zibrov, M. Endres, M. Greiner, *et al.*, Probing many-body dynamics on a 51-atom quantum simulator, *Nature* **551**, 579 (2017).
- [39] A. Polkovnikov, K. Sengupta, A. Silva, and M. Vengalattore, Colloquium: Nonequilibrium dynamics of closed interacting quantum systems, *Rev. Mod. Phys.* **83**, 863 (2011).
- [40] T. W. Kibble, Topology of cosmic domains and strings, *Journal of Physics A: Mathematical and General* **9**, 1387 (1976).
- [41] J. Dziarmaga, Dynamics of a quantum phase transition: Exact solution of the quantum Ising model, *Phys. Rev. Lett.* **95**, 245701 (2005).
- [42] J. S. Langer, Statistical theory of the decay of metastable states, *Annals of Physics* **54**, 258 (1969).
- [43] I. Affleck, Quantum-statistical metastability, *Phys. Rev. Lett.* **46**, 388 (1981).
- [44] A. O. Caldeira and A. J. Leggett, Influence of dissipation on quantum tunneling in macroscopic systems, *Phys. Rev. Lett.* **46**, 211 (1981).
- [45] A. J. Leggett, Quantum tunneling in the presence of an arbitrary linear dissipation mechanism, *Phys. Rev. B* **30**, 1208 (1984).
- [46] A. J. Leggett, S. Chakravarty, A. T. Dorsey, M. P. A. Fisher, A. Garg, and W. Zwerger, Dynamics of the dissipative two-state system, *Rev. Mod. Phys.* **59**, 1 (1987).
- [47] P. Hänggi, P. Talkner, and M. Borkovec, Reaction-rate theory: fifty years after Kramers, *Rev. Mod. Phys.* **62**, 251 (1990).
- [48] S. Birkammer, A. Bastianello, and M. Knap, Prethermalization in one-dimensional quantum many-body systems with confinement, *Nat. Commun.* **13**, 7663 (2022).
- [49] P. Fendley, K. Sengupta, and S. Sachdev, Competing density-wave orders in a one-dimensional hard-boson model, *Phys. Rev. B* **69**, 075106 (2004).
- [50] I. Lesanovsky and H. Katsura, Interacting Fibonacci anyons in a Rydberg gas, *Phys. Rev. A* **86**, 041601(R) (2012).
- [51] C. J. Turner, A. A. Michailidis, D. A. Abanin, M. Serbyn, and Z. Papić, Weak ergodicity breaking from quantum many-body scars, *Nat. Phys.* **14**, 745 (2018).
- [52] G.-X. Su, H. Sun, A. Hudomal, J.-Y. Desautels, Z.-Y. Zhou, B. Yang, J. C. Halimeh, Z.-S. Yuan, Z. Papić, and J.-W. Pan, Observation of many-body scarring in a Bose-Hubbard quantum simulator, *Phys. Rev. Res.* **5**, 023010 (2023).
- [53] F. Balducci, A. Gambassi, A. Leroze, A. Scardicchio, and C. Vanoni, Localization and melting of interfaces in the two-dimensional quantum ising model, *Phys. Rev. Lett.* **129**, 120601 (2022).

- [54] O. Hart and R. Nandkishore, Hilbert space shattering and dynamical freezing in the quantum ising model, [Phys. Rev. B **106**, 214426 \(2022\)](#).
- [55] R. M. Karp, Reducibility among combinatorial problems, in *Complexity of Computer Computations*, The IBM Research Symposia Series, edited by R. E. Miller, J. W. Thatcher, and J. D. Bohlinger (Springer US, Boston, MA, 1972) pp. 85–103.
- [56] H.-P. Breuer and F. Petruccione, *The Theory of Open Quantum Systems* (Oxford University Press, 2007).
- [57] U. Schollwöck, The density-matrix renormalization group in the age of matrix product states, [Annals of Physics **326**, 96 \(2011\)](#).
- [58] G. Vidal, Efficient classical simulation of slightly entangled quantum computations, [Phys. Rev. Lett. **91**, 147902 \(2003\)](#).
- [59] S. Paeckel, T. Köhler, A. Swoboda, S. R. Manmana, U. Schollwöck, and C. Hubig, Time-evolution methods for matrix-product states, [Annals of Physics **411**, 167998 \(2019\)](#).